Biomaterials 288 (2022) 121710

Contents lists available at ScienceDirect

Biomaterials

journal homepage: www.elsevier.com/locate/biomaterials

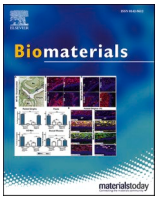

Adhesive peptide and polymer density modulate 3D cell traction forces within synthetic hydrogels

Mark Colasurdo [a,b], Elisa B. Nieves [a,b], Marc A. Fernández-Yagüe [b,c], Christian Franck [d], Andrés J. García [b,c,*]

[a] Wallace H. Coulter Department of Biomedical Engineering, Georgia Institute of Technology and Emory University, Atlanta, GA, 30332, USA
[b] Parker H. Petit Institute for Bioengineering and Bioscience, Georgia Institute of Technology, Atlanta, GA, 30332, USA
[c] George W. Woodruff School of Mechanical Engineering, Georgia Institute of Technology, Atlanta, GA, 30332, USA
[d] Department of Mechanical Engineering, University of Wisconsin-Madison, Madison, WI, USA

ARTICLE INFO

Keywords:
mechanotransduction
Integrins
Cytoskeleton
Contractility
Vinculin

ABSTRACT

Cell-extracellular matrix forces provide pivotal signals regulating diverse physiological and pathological processes. Although mechanobiology has been widely studied in two-dimensional configurations, limited research has been conducted in three-dimensional (3D) systems due to the complex nature of mechanics and cellular behaviors. In this study, we established a platform integrating a well-defined synthetic hydrogel system (PEG-4MAL) with 3D traction force microscopy (TFM) methodologies to evaluate deformation and force responses within synthetic microenvironments, providing insights that are not tractable using biological matrices because of the interdependence of biochemical and biophysical properties and complex mechanics. We dissected the contributions of adhesive peptide density and polymer density, which determines hydrogel stiffness, to 3D force generation for fibroblasts. A critical threshold of adhesive peptide density at a constant matrix elasticity is required for cells to generate 3D forces. Furthermore, matrix displacements and strains decreased with matrix stiffness whereas stresses, and tractions increased with matrix stiffness until reaching constant values at higher stiffness values. Finally, Rho-kinase-dependent contractility and vinculin expression are required to generate significant 3D forces in both collagen and synthetic hydrogels. This research establishes a tunable platform for the study of mechanobiology and provides new insights into how cells sense and transmit forces in 3D.

1. Introduction

Cell-extracellular matrix (ECM) mechanotransduction is a process mediated by integrin-based adhesions and the cytoskeleton by which mechanical forces are converted into biochemical signals [1–3]. Cellular traction forces allow cells to sense the biophysical and biochemical properties of the surrounding matrix and thus regulate fundamental cellular processes such as proliferation, differentiation, and migration, as well as more complex processes including morphogenesis, pathogenesis, and tissue repair [4–7]. Mechanotransduction considerations are also important to biomaterials design, tissue engineering, and regenerative medicine [8–10].

Although mechanobiology has been widely studied in two-dimensional (2D)/planar configurations, limited research has been conducted in three-dimensional (3D) systems due to the complex nature of mechanics and cellular behavior in these systems as well as technical limitations. Nevertheless, understanding cellular behaviors in 3D is critical because most cell types operate in 3D microenvironments within the body, and it is possible that cells mechanically interact with their ECM in fundamentally different ways in 2D vs. 3D [11–13]. In recent years, 3D Traction Force Microscopy (3D TFM) has been developed to estimate cell-generated forces in 3D [14–22]. 3D TFM studies have demonstrated that cells conserve some aspects of 2D mechanotransduction, while deviating in other ways in 3D. For example, 3D TFM studies have shown force transmission via a cytoskeletal clutch for fibroblasts, heterogeneous deformation patterns for epithelial multicellular aggregates, and even constant forces independent of matrix density and pulsatile contractile force-driven migration for breast carcinoma cells [23–25].

The large majority of experimental systems used for TFM employ biologically-derived matrices, such as collagen and fibrin, which provide poor control over the biophysical and biochemical properties of the

* Corresponding author. Parker H. Petit Institute for Bioengineering and Bioscience, Georgia Institute of Technology, Atlanta, GA, 30332, USA.
E-mail address: andres.garcia@me.gatech.edu (A.J. García).

https://doi.org/10.1016/j.biomaterials.2022.121710
Received 11 March 2022; Received in revised form 27 July 2022; Accepted 31 July 2022
Available online 11 August 2022

matrix [23–26]. These biologically-derived matrices do not permit independent tuning of biophysical and biochemical parameters, such as matrix rigidity and ligand density, and are often difficult to mechanically model due to the complex and anisotropic nature of their fibrillar architecture. For these reasons, biological matrices limit the study of specific cell-matrix interactions and thus may obfuscate insights that could be obtained from engineered matrix systems. On the other hand, synthetic hydrogels enable modular and independent control over matrix properties like polymer density and ligand density and also facilitate mechanical modelling as these materials have more defined (e.g., isotropic) mechanical behavior [27–31]. Thus, the use of 3D synthetic hydrogels provides a platform that is precisely engineered, enabling a more robust and quantitative study of mechanobiology in cells.

Herein, we describe the use of 3D synthetic hydrogels based on a 4-armed poly (ethylene glycol) macromer functionalized with maleimide groups at the end of each arm (PEG-4MAL) and 3D TFM to study the cellular force response to matrix properties in 3D. Murine embryonic fibroblasts (MEFs) were encapsulated and cultured within hydrogels with varying ligand type, polymer density, and actomyosin contractility modulation. Under these conditions, we analyzed numerous metrics of cell-generated deformations using 3D TFM and a cross-correlation algorithm to track deformations within these linearly elastic gels. We found that a critical threshold of adhesive peptide density at a constant matrix elasticity is required for cells to generate 3D forces. We also found that polymer density, which determines the mechanical properties of the hydrogel, modulates cellular morphology and the magnitude of cell-generated stresses for a constant ligand density. Finally, we confirmed that cell contractility and vinculin expression are required in MEFs to generate significant 3D forces in both biological and synthetic materials. This research establishes a tunable platform for the study of mechanobiology and provides new insights into how cells sense and transmit forces in 3D.

2. Materials and methods

2.1. Cell culture

MEFs were cultured in FluoroBrite DMEM supplemented with 10% fetal bovine serum and antibiotics (penicillin/streptomycin) at 37 °C and 5% CO_2 and passaged using trypsin following standard protocols. Prior to encapsulation, cells were stained with CellTracker Red to facilitate visualization and image analysis.

2.2. 3D PEG-4MAL hydrogels and cell encapsulation

PEG-4MAL hydrogels presenting adhesive peptide and crosslinked with a protease-degradable peptides were prepared as described before with minor modifications [28,32]. PEG-4MAL macromer (20 kDa, >95% purity, Laysan Bio), adhesive peptide, and crosslinking peptide were weighed to stoichiometrically appropriate quantities and then dissolved in PBS containing both calcium and magnesium. Once dissolved, peptides were titrated to pH 6.5–6.8. Next, GRGDSPC (RGD, AAPPTEC) adhesive peptide or its inactive control peptide GRDGSPC (RDG, AAPPTEC) was reacted with PEG-4MAL to yield functionalized macromer. Yellow-green fluorescent beads (500 nm diameter, FluoSpheres) were added to the PEG-RGD solution at a 1:50 beads:PEG-RGD volumetric ratio. MEFs stained with 7 μM CellTracker Red were then added to the PEG-RGD-bead solution at a final concentration of 100,000 cells/mL. Once cells are dispersed within the precursor solution, the protease-degradable peptide GCRDVPMSMRGGDRCG (VPM, AAPPTEC) was added to crosslink the components into a hydrogel. We used Ibidi micro-Slide III 3D Perfusion slides, which contain 6 wells for 3D hydrogel culture. To polymerize the gels in this platform, the VPM solution was first added to each of the 6 wells. Then the precursor solution containing cells was added to the crosslinking solution and gently pipetted up-and-down to mix and polymerize the gels. The gels were then incubated at room temperature for 10 min before media was added. The encapsulated cells were cultured in the slides for 2 days in a cell culture incubator prior to microscopy.

2.3. Rheology

Mechanical characterization of hydrogels was performed using an Anton-Paar cone-and-plate rheometer. Gels synthesized for mechanical testing were swollen in PBS containing both calcium and magnesium for 2 days at room temperature. Amplitude sweeps were performed from 0.1% to 10% strain to estimate the linear viscoelastic regime of the gels. Based on the amplitude sweeps, a constant strain of 1% was applied during subsequent frequency sweeps, which ranged from 0.1 to 10 rad/s. The frequency sweeps provide information on the storage and loss moduli and how they change under varying strain rate. The storage modulus reported here was the average of the storage moduli measured at each frequency point.

2.4. 3D traction force microscopy

Traction Force Microscopy was performed using a Nikon Eclipse Ti inverted microscope equipped with a C2 laser scanning confocal head with a 40× water-immersion objective (NA = 1.15; X–Y resolution ≈ 0.20 μm). Prior to imaging, the microscope and live-cell imaging chamber were allowed reach 37 °C for 1 h to minimize thermal drift. In addition, 5% CO_2 was delivered to the live-cell incubator and allowed to reach equilibrium. Likewise, once the microscope reached temperature, the slide was then set in the live-cell incubator and allowed to come to thermal equilibrium for an additional hour to minimize thermal drift within the sample.

Single cells with no neighboring cells within 50 μm and at least 200 μm from the bottom surface of the chamber (to avoid edge effects on hydrogel stiffness) were selected for analysis. Traction Force Microscopy was conducted via a time series of z-stacks. The time series consisted of 6 z-stacks taken every 10 min, with each z-stack spanning 80 μm with a spacing of 0.8 μm, resulting in an image that was 512 × 512 x 101 voxels and 6 time points. Once the initial stack of the stressed state was acquired (t = 0), the series would be paused to allow for laser ablation of the cell to disengage the cell from the matrix. Laser ablation was performed by zooming in on the cell body 25× and continuously scanning the cell with the 561 nm laser at 80% power for 5 min. Immediately upon completion of ablation, the next z-stack (t = 1) was taken and the time series resumed as normal until all 6 time points were captured.

To estimate the deformation fields generated by the cells, we used a digital volume correlation (DVC) algorithm developed by Franck et al. to measure the motion of beads between time points [15,33,34]. We built a MATLAB workflow to measure matrix displacements, transform them into mechanical fields, and measure morphological properties of cells. Using Franck's Fast Iterative DVC algorithm, which is an enhanced DVC that takes advantage of iterative rounds of correlation to not only improve the algorithm's ability to converge on accurate deformation measurements but also reduces the computational cost of the algorithm. Importantly, the DVC algorithm is a significant advancement in solving inverse mechanical problems because it does not require the regularization of a nodal system that is necessary for finite element analysis. Instead, because the voxels serve as a gridded system in and of itself, displacement values from DVC can be directly transformed into downstream mechanical values such as strain and stress.

To translate displacement fields into stress fields, a constitutive model based in continuum mechanics is typically used. In previous work, Franck has shown that cells are capable of generating significant amounts of strain, sometimes up to 40%, which would invalidate many assumptions of infinitesimal strain and linear elasticity [33]. As such, a finite strain theory is more appropriate for describing the mechanics within biological tissues and polymeric matrices, as they often undergo plastic and viscoelastic deformation. The Green-Lagrangian strain

tensor, **E**, is often used to describe strain in continua beyond infinitesimal strain and can be defined as a function of the deformation gradient, **F** [33].

The Green-Lagrangian strain is defined as (1):

$$\mathbf{E} = \frac{1}{2}\left(\mathbf{F}^{\mathrm{T}}\mathbf{F} - \mathbf{I}\right) \tag{1}$$

where the deformation gradient is defined as a function of the displacement gradient (2):

$$\mathbf{F} = \mathbf{I} + \nabla\mathbf{u} \tag{2}$$

and where the displacement gradient is defined as (3):

$$\nabla\mathbf{u} = \frac{\delta\mathbf{u}_i}{\delta\mathbf{x}_j} \tag{3}$$

In order to calculate stresses, the mechanical properties of the material must be defined. The shear modulus, G, of PEG-4MAL hydrogels was derived from the storage (G′) and loss (G″) moduli of the material from rheology. We selected a nearly incompressible (Poisson's ratio, $\nu = 0.45$) neo-Hookean model, which is able to accommodate strains of up to 20% [33]. Previous 3D TFM publications have used similar assumptions of neo-Hookean behavior and $\nu = 0.45$ [21,22,35].

The neo-Hookean constitutive equation is described as (4):

$$\sigma = \frac{\mu}{\mathbf{J}^{\frac{5}{3}}}\left(\mathbf{B} - \frac{1}{3}\mathrm{trace}(\mathbf{B})\cdot\mathbf{I}\right) + \mathrm{K}(\mathrm{J}-1)\mathbf{I} \tag{4}$$

where μ, the shear modulus, is equal to the storage modulus G' (for an elastic material), and K, the bulk modulus, is related to G' and Poisson's ratio, ν by (5):

$$\mathrm{K} = \frac{2\mathrm{G}'(1+\nu)}{3(1-2\nu)} \tag{5}$$

and J, the Jacobian of **F**, and **B**, the left Cauchy Green's tensor, are defined as (6,7):

$$\mathrm{J} = \det\mathbf{F} \tag{6}$$

$$\mathbf{B} = \mathbf{F}\mathbf{F}^{\mathrm{T}} \tag{7}$$

This approach allows us to describe large deformations within a continuum mechanics framework, providing metrics for quantification and statistical analysis.

To quantify different aspects of cell-generated deformations, we developed and implemented several output metrics ranging from displacement through stress. The segmented volume of the cell, based on its CellTracker signal, was used to determine which values in the deformation field to include in calculations in the subsequent metrics. Although the volume of the cell is used as the inclusion-exclusion criterion, it must be emphasized that all quantifications are based on deformations of the matrix, not the cell. The cell volume is simply a convenient method for quantifying sub-full-field deformations. The voxels in the deformation fields that coincided with the cell volume were included, while everything outside the volume of the cell was excluded. We note that increasing the inclusion area around the cell, via dilation of the binary image, was tested, but showed no difference in the interpretation of data and only increased the chance of including non-specific information in our calculations, thus only the matrix deformations coinciding with the volume of the cell were included.

The displacement field was used to calculate mean and max displacements, meanU and maxU, respectively. These values represent the average matrix displacements and the maximum matrix displacements. These values were taken from the resultant displacement field R, which is calculated element-wise by (8):

$$\mathrm{R} = \sqrt{\mathrm{u}_x^2 + \mathrm{u}_y^2 + \mathrm{u}_z^2} \tag{8}$$

The strain field was computed by first determining the Green-Lagrangian strain tensor $\mathbf{E}(i,j,k)$ for each voxel in the displacement field, where (9):

$$\mathbf{E}(i,j,k) = \frac{1}{2}\left(\mathbf{F}(i,j,k)\cdot\mathbf{F}(i,j,k)^{\mathrm{T}} - \mathbf{I}\right) \tag{9}$$

and the deformation tensor is defined as (10):

$$\mathbf{F}(i,j,k) = \mathbf{I} + \nabla\mathbf{u}(i,j,k) = \begin{bmatrix} 1+\frac{du_x}{dX}(i,j,k) & \frac{du_x}{dY}(i,j,k) & \frac{du_x}{dZ}(i,j,k) \\ \frac{du_y}{dX}(i,j,k) & 1+\frac{du_y}{dY}(i,j,k) & \frac{du_y}{dZ}(i,j,k) \\ \frac{du_z}{dX}(i,j,k) & \frac{du_z}{dY}(i,j,k) & 1+\frac{du_z}{dZ}(i,j,k) \end{bmatrix} \tag{10}$$

Once each voxel has a defined strain tensor, this representation of strain was converted into a scalar value for quantification of descriptive statistics. To do this, the principal strains E_p of each tensor were computed by determining its eigenvalues (11):

$$\mathbf{E}_p(i,j,k) = [\,\lambda_x(i,j,k) \quad \lambda_y(i,j,k) \quad \lambda_z(i,j,k)\,] \tag{11}$$

A scalar value is reached by computing the magnitude of the principal strains (12):

$$\mathbf{E}_p(i,j,k) = \sqrt{\lambda_x(i,j,k)^2 + \lambda_y(i,j,k)^2 + \lambda_z(i,j,k)^2} \tag{12}$$

Thus, the magnitude of the principal strains at each voxel is subsequently used to determine the mean strain (meanE) and max strain (maxE) in those voxels that coincide with the cell volume.

Stress was computed in an analogous manner to strain by first determining the Cauchy stress tensor for each voxel in the image, $\boldsymbol{\sigma}(i,j,k)$ (13):

$$\boldsymbol{\sigma}(i,j,k) = \frac{\mu}{\mathbf{J}(i,j,k)^{\frac{5}{3}}}\left(\mathbf{B}(i,j,k) - \frac{1}{3}\mathrm{trace}(\mathbf{B}(i,j,k))\cdot\mathbf{I}\right) + \mathrm{K}(i,j,k)(\mathrm{J}(i,j,k)-1)\mathbf{I} \tag{13}$$

Then, the principal stresses $\boldsymbol{\sigma}_p(i,j,k)$ were determined by finding the eigenvalues at each voxel (14):

$$\boldsymbol{\sigma}_p(i,j,k) = [\,\lambda_x(i,j,k) \quad \lambda_y(i,j,k) \quad \lambda_z(i,j,k)\,] \tag{14}$$

Finally, scalar values are derived from the magnitude of the principal stresses at each voxel (15):

$$\boldsymbol{\sigma}_p(i,j,k) = \sqrt{\lambda_x(i,j,k)^2 + \lambda_y(i,j,k)^2 + \lambda_z(i,j,k)^2} \tag{15}$$

The mean, max, and total stress, meanS, maxS, and totS, are computed respectively thereafter.

In addition to principal stress, traction stress **T** was computed at each voxel at the surface of the cell. The normal vectors **n** are determined for each voxel at the perimeter of the segmented cell volume by taking the gradient of the surface of the cell. Tractions are then computed by (16):

$$\mathbf{T}(i,j,k) = \boldsymbol{\sigma}(i,j,k)\cdot\mathbf{n}(i,j,k) \tag{16}$$

And a scalar value is produced for tractions by computing the magnitude of the traction vector (17):

$$\mathrm{T}(i,j,k) = \sqrt{\mathrm{T}_x(i,j,k)^2 + \mathrm{T}_y(i,j,k)^2 + \mathrm{T}_z(i,j,k)^2} \tag{17}$$

Mean, max, and total tractions (meanT, maxT, and totT) were computed for the voxels that coincide with the cell surface.

Strain energy density, the amount of energy required to strain the material per unit volume, was computed. For a nearly incompressible ($\nu = 0.45$), neo-Hookean material, strain energy density is defined as a function of the left Cauchy-Green deformation tensor, Jacobian, shear modulus, and bulk modulus of the material (18,19):

$$\mathbf{W} = \frac{\mu}{2}\left(\frac{\mathrm{trace}(\mathbf{B})}{\mathbf{J}^{\frac{2}{3}}} - 3\right) + \frac{\mathrm{K}}{2}(\mathrm{J}-1)^2 \tag{18}$$

where W is the strain energy density, μ is the material's shear modulus, K is the material's bulk modulus, J is the Jacobian, and B is the left Cauchy-Green deformation tensor. For our calculations, the storage modulus of the material, G′, is substituted for μ. To obtain a value appropriate for statistics, such as meanW and maxW, we simply take the absolute value of the strain energy density field (20):

$$|\mathbf{W}|(\mathrm{i},\mathrm{j},\mathrm{k}) = \left|\frac{\mu}{2}\left(\frac{\mathrm{trace}(\mathbf{B})}{\mathbf{J}^{\frac{2}{3}}} - 3\right) + \frac{\mathrm{K}}{2}(\mathrm{J}-1)^2\right| \tag{19}$$

Finally, to obtain strain energy, strain energy density was multiplied by the differential volume of each voxel and integrated across the entire volume of the cell. Similar to strain energy density, the absolute value of the strain energy was used for statistical analyses.

Polar contour plots are generated by rotating, aligning, and averaging the deformation fields. Cell-to-cell variability in shape, protrusions, and focal adhesion may result in perceived anisotropy within the polar contour plots.

2.5. Live cell microscopy

PEG-4MAL hydrogels containing eGFP-vinculin-expressing fibroblasts [36] were cast into Ibidi micro-Slide III 3D Perfusion slides as previously described and cultured for 2 days prior to imaging. Live cell microscopy was performed using a PerkinElmer UltraVIEW VoX spinning disk confocal system mounted on a Nikon Ti-E Eclipse inverted microscope with a 40× water-immersion objective (NA = 1.15; X–Y resolution ≈ 0.20 μm). Images were recorded with an EM-CCD camera (C9100-23b back-thinned EMCCD, Hamamatsu, Tokyo, Japan) using a 488-nm argon krypton laser (power 90%, exposure time 850 ms). For each cell, z-stack raw images of 1 μm optical thickness for a total height of 50 μm were taken. Volocity imaging software (Perkin Elmer) was used to perform uniform contrast adjustments, and generate the final composite images, which represent the maximum intensity projections of the z-stacks.

2.6. Statistics

All experiments were performed on biological replicates. Outliers were first removed from all datasets using the ROUT method (Q = 10%). Normally distributed data that presented equal variances was analyzed via one-way ANOVA. All other data that did not present a Gaussian distribution or homoscedasticity was analyzed by non-parametric Kruskal-Wallis test. A p-value < 0.05 was considered significant. All analyses were performed using Prism 8.4 (GraphPad Software, San Diego, CA).

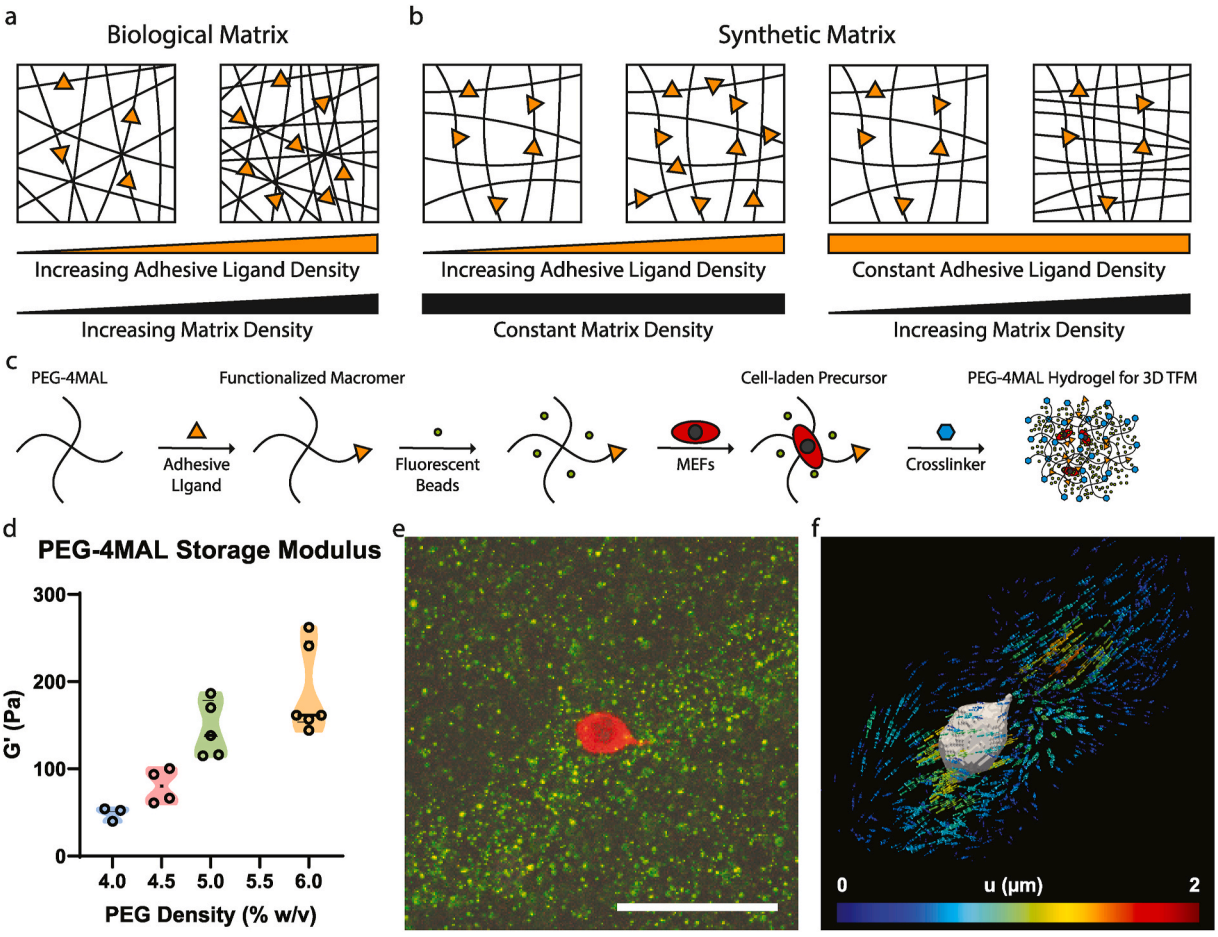

Fig. 1. Overview of PEG-4MAL 3D TFM System. (a) Biological matrices have coupled ligand and polymer density. (b) PEG-4MAL hydrogel has independently tunable adhesive ligand and polymer densities. (c) Synthesis of PEG-4MAL hydrogels for 3D TFM (not drawn to scale). (d) Storage modulus for PEG-4MAL hydrogel of varying polymer densities. (e) Confocal image of CellTracker-stained cell surrounded by fluorescent beads in 3D PEG-4MAL hydrogel. Scale bar = 50 μm. (f) 3D visualization of displacement field surrounding the same cell from panel e.

3. Results

3.1. 3D traction force microscopy in synthetic hydrogels

3D TFM has become an important tool in the study of 3D cellular mechanobiology [15,16,37,38]. Prior 3D TFM studies have primarily relied on the use of biological matrices such as collagen and fibrin, which lack independent control over matrix protein density (which influences mechanical properties and fiber architecture) and adhesive ligand density, two key features pertinent to force generation within matrices (Fig. 1a). Therefore, the contributions of ECM biophysical and biochemical properties to 3D forces cannot be rigorously analyzed. Unlike biological matrices, synthetic PEG-4MAL hydrogels allow for independent tuning of polymer and adhesive peptide densities, thus enabling the separate study of biophysical and biochemical properties (Fig. 1b). The PEG-4MAL platform outperforms free-radical polymerization and other Michael-type addition chemistries in generating structurally-defined hydrogels with stoichiometric incorporation of bioligands, improved crosslinking efficiency, and excellent *in vitro* and *in vivo* cytocompatibility [28,32,39]. Importantly, in this synthetic platform, polymer density, adhesive peptide type and density, and crosslinker type and density can be independently controlled to tune hydrogel mechanical properties, adhesive peptide presentation, and protease-dependent degradation. To synthesize hydrogels for 3D TFM, PEG-4MAL macromer was first reacted with a cysteine-containing RGD cell adhesive peptide to generate a functionalized macromer (Fig. 1c). Next, a high density of 500 nm diameter fluorescent beads, which serve as fiduciary markers for deformation tracking, was dispersed within the hydrogel precursor solution. Finally, cells stained with CellTracker Red were added and the hydrogels were polymerized using protease-degradable VPM crosslinking peptide such that the cells are encapsulated within the 3D matrix. PEG-4MAL hydrogels provide defined control over the bulk mechanical properties, such as the storage modulus (G', which is directly proportional to the elastic modulus), and the mechanical properties can be simply tuned by varying the polymer density while maintaining constant RGD density (Fig. 1d). Rheological analyses demonstrated that the PEG-4MAL hydrogel platform behaves as a linearly elastic material (Figure S1). MEFs were cultured for 2 days in the hydrogels and then observed under live-cell confocal microscopy (Fig. 1e). 3D TFM was then performed by disrupting the mechanical state of the cell via localized laser ablation and acquiring a time series of 3D z-stacks to capture any resulting deformations within the gel. Mechanical deformations were then computed from the 3D time series using a digital volume correlation (DVC) algorithm, which tracks displacements of the fluorescent beads from the stressed state (t = 0) to the relaxed state (t = relaxed) of the cell (Fig. 1f). Finally, scalar values representing mean, max, and total metrics (displacement, strain, stress, traction, strain energy) were calculated.

As 3D TFM has not yet been performed in PEG-4MAL hydrogels, we first characterized and validated several key features of the system. First, we examined cell viability for encapsulated MEFs. Within the 3D synthetic hydrogels, viability typically exceeded 90% over multiple days (Figure S2). Cells were able to spread and proliferate at lower PEG-4MAL polymer densities (4.0–6.0%), which is consistent with other studies indicating that fibroblasts spread more frequently in lower density gels as there is less physical confinement [28,40–42]. Next, we developed a method to disengage cells from the hydrogel to obtain a non-stressed state of the surrounding matrix (Figure S3). Traditionally, TFM studies use detergents to lyse cells or cytoskeletal inhibitors to disrupt contractility in bulk [16,23,25,33], but these approaches pose practical challenges. For instance, adding detergent to a sample does not selectively target cells, has variable timing (as long as 2 h) and effectiveness depending on detergent transport, and addition of the disruptive agents can introduce motion artifacts. We instead used a 561 nm laser to selectively photo-ablate cells with high spatiotemporal precision without motion artifacts [43,44]. The 561 nm laser was selected as it does not photobleach the fluorescent yellow-green beads used for deformation tracking. Micro-rheology, a technique used to estimate the mechanical properties of soft materials by measuring the Brownian motion of entrapped particles, was performed on gels to determine whether laser application alters the mechanical properties of the gel (e.g., by local heating) (Figure S4). Using 200 nm diameter FluoSpheres, the slope of the mean squared displacement, represented by α, indicates that mechanical properties of the gels are not affected by the laser ablation. No change is to be expected, as the hydrogels are optically transparent and thus unlikely to absorb a large amount of energy from the laser. Through optimization experiments, we determined that laser ablation at 80% power for 5 min reliably produces cell swelling and blebbing followed by retraction of cell processes, indications that the cytoskeleton has been disrupted and disengaged from the matrix. Lastly, we characterized the time-course over which the matrix relaxes post-ablation. For full relaxation to be captured, we imaged the cells over the course of 45 min, taking image stacks every 10 min (Figure S5). These time points not only facilitate accurate reconstruction of the displacement field, but also enable more accurate image registration over the course of matrix relaxation. Taken together, these results validate a methodology to perform 3D TFM within PEG-4MAL hydrogels.

3.2. ROCK inhibition attenuates 3D matrix deformations and forces

We expect that actomyosin contractility is required for cell-generated forces to deform the matrix based on previous literature with biological matrices [45,46]. To examine the role that the actomyosin cytoskeleton plays in generating cellular traction forces within 3D PEG hydrogels, we treated cells within gels with the Rho-associated protein kinase (ROCK) inhibitor, Y-27632, which disrupts myosin contractility similar to blebbistatin, but is preferable due to the phototoxicity of blebbistatin [47]. Cells were initially encapsulated in 4.5% PEG-4MAL gels functionalized with 2.0 mM RGD, as this formulation has been previously shown to yield high cell viability [28]. After 1 day, culture media was exchanged with control media (no inhibitor) or treated media, containing 10 μM Y-27632.3D TFM was performed the following day, after cells had been exposed to control and treatment conditions for 24 h to allow for sufficient diffusion and equilibration of inhibitor (Fig. 2a and b). Cell morphology, as assessed by cell polarity and volume, was not altered by Y-27632 treatment, likely due to the existence of integrin-RGD bonds prior to Y-27632 treatment (Fig. 2e and f). However, treatment with the ROCK inhibitor greatly reduced the range of cell polarity, disabling the cells' ability to form stable enough tractions to maintain polarized configurations.

We found that several metrics of 3D matrix deformation and mechanics were reduced in cells treated with the ROCK inhibitor compared to untreated cells. To obtain a sense of the distribution of material deformations relative to the cell, we rotated, aligned, and averaged the deformation fields across all cells for a given condition to yield polar contour plots (Fig. 2c and d). Untreated cells show larger in-plane deformation fields, extending to 30 μm beyond the centroid of the cell in its principal directions, while strain and stress fields are more localized to the center of the cell. Similarly, Y-27632-treated cells show polarized displacements along the principal axis of the cell, with centralized strain and stress fields, although these deformations do not extend as far as those in the untreated control.

We quantified matrix deformations that cells generated. Control cells generated larger mean and max displacements within the gel compared to Y-27632-treated cells (Fig. 2g and h). However, no differences in strain metrics were observed between control and Y-27632-treated cells (Fig. 2i and j). This result indicates that, while displacements are greater in control conditions, the amount of strain applied to the matrix was equivalent between the conditions, meaning that control and treated cells generated relatively uniform displacement fields but with different magnitudes.

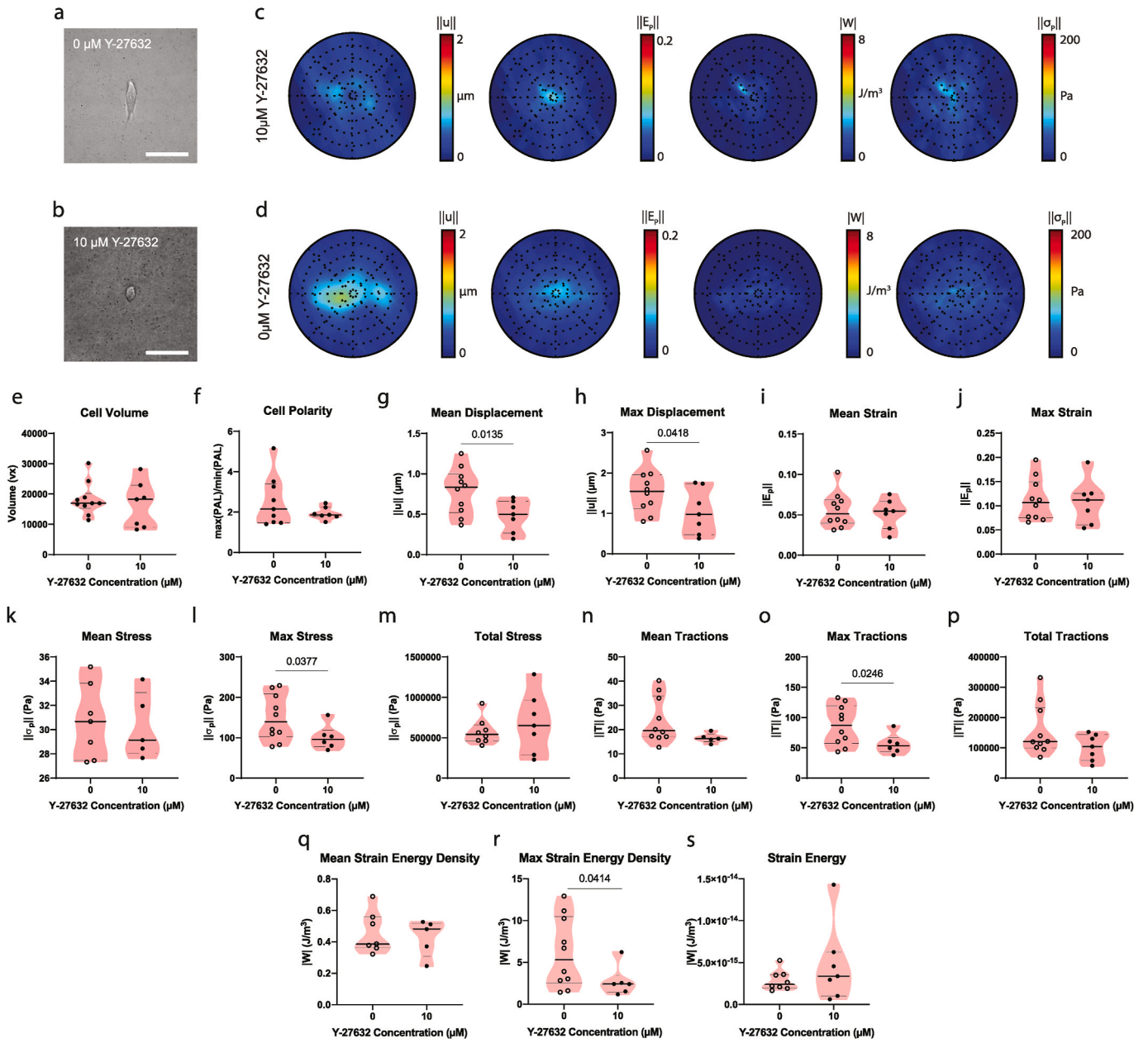

Fig. 2. Treatment with Y-27632 reduces 3D forces in PEG-4MAL hydrogels. Images of (a) control and (b) Y-27632 (10 μM)-treated cells in 4.5% PEG-4MAL hydrogel. Scale bar 50 μm. (c) Polar contour plots displaying the average displacement, strain, stress, and strain energy density fields for control untreated cells. Graticules spaced at 10 μm apart. (d) Polar contour plots displaying the average displacement, strain, stress, and strain energy density fields for Y-27632-treated cells. Graticules spaced at 10 μm apart. (e) Cell volume. (f) Cell polarity. (g) Mean and (h) maximum matrix displacements quantified within the cell volume. (i) Mean and (j) maximum matrix strain quantified within the cell volume. (k) Mean, (l) maximum, and (m) total matrix stresses quantified within the cell volume. (n) Mean, (o) maximum, and (p) total matrix tractions quantified at the cell surface. (q) Mean and (r) maximum strain energy density quantified within the cell volume. (s) Strain energy.

We also quantified stresses, tractions, and strain energy applied to the matrix by untreated and ROCK-inhibited cells. Principal stresses are used to quantify the continuous stress field surrounding a cell, while tractions quantify the amount of stress generated perpendicular to a cell's surface. Strain energy represents the amount of energy required to deform the matrix based on the material's modulus. The principal stress field across the cell demonstrates that untreated cells generate higher maximum stresses compared to Y-27632-treated cells, demonstrating that ROCK activity and cell contractility are necessary for cells to generate large matrix forces within these synthetic gels (Fig. 2k–m). The same pattern is seen with regard to traction stresses, with the range of mean and max tractions reduced in Y-27632-treated cells (Fig. 2n–p). Lastly, ROCK inhibition reduced the maximum strain energy density applied to the matrix by cells, but no differences were detected for mean strain energy density or strain energy within the system (Fig. 2q–s). These results demonstrate that ROCK-dependent cell contractility is required for large matrix deformation and maximal force generation without affecting cellular morphology within PEG-4MAL hydrogels.

3.3. *Threshold adhesive ligand density is required for 3D forces*

To investigate the contribution of adhesive peptide density to 3D traction forces, MEFs were cultured within 4.5% PEG-4MAL hydrogels containing a range of RGD concentrations: 0.0, 0.5, 1.0, and 2.0 mM

RGD (Fig. 3a–d). To maintain equivalent hydrogel nanostructure and mechanical properties among adhesive groups, RGD was combined with its non-adhesive analog, RDG, such that the combination of adhesive and non-adhesive peptide was kept constant at 2.0 mM. Experiments performed using 2.0 mM RDG non-adhesive peptide showed low values for all metrics indicating that cell adhesion to the RGD peptide coupled to the hydrogel network is primarily responsible for the observed deformation and that the proteases and matrix proteins secreted at the gel-cell interface have minimal influence on the 3D TFM methodology. Despite the differences in RGD concentrations, no significant differences were observed in cellular morphology according to cell volume and polarity (Fig. 3i and j). Cell polarity does not change with increasing ligand density, which is counter to previous work on planar substrates that demonstrates that cell polarity increases with ligand density [48, 49]. However, the range of polarity values increases in 2.0 mM RGD gels, indicating that while most cells were similarly rounded as those in lower RGD densities, the 2.0 mM RGD ligand density supported the presence of more spread cells.

Despite the lack of polarization, cells in 2.0 mM gels generated larger deformation fields than in those in gels with lower RGD densities. For both 0.0 and 0.5 mM RGD gels, little to no matrix deformation was observed in the central plane of the cell, indicating that minimal deformation occurs at these ligand densities (Fig. 3e and f). Small amounts of matrix strain, strain energy, and stress values were observed for 1.0 mM RGD gels (Fig. 3g). Strikingly, large amounts of displacement, strain, strain energy, and stress values were evident for the 2.0 mM RGD group (Fig. 3h).

To quantify the deformation fields, displacement and strain values that overlapped with the cell body were used to compute mean and max displacements. In agreement with the polar contour plots, cells in 2.0 mM RGD gels exerted significantly larger mean and maximum matrix displacements (Fig. 3k,l) as well as higher mean and maximum strain on the surrounding matrix compared to 0, 0.5, and 1.0 mM RGD conditions (Fig. 3m,n).

Consistent with the displacement and strain results, we found that MEFs in 2.0 mM RGD gels produced larger principal and traction stresses compared to cells encapsulated in gels with lower concentrations of RGD (Fig. 3o–t). Because this synthetic system has constant matrix mechanical properties, it is expected that greater stresses are required to generate larger deformations. Likewise, strain energy density and strain energy are significantly increased in the 2.0 mM RGD group compared to all others, indicating that greater energy is required to deform the matrix as well (Fig. 3u–w). These results demonstrate that 2.0 mM RGD density is required for cells to apply ~10–20 J/m^3 strain energy density and 200–300 Pa of stress on PEG-4MAL gels, demonstrating that a critical density of adhesive ligand is required for cells to transmit sufficient integrin-mediated 3D forces and deform the surrounding matrix.

We posited that the observed adhesive ligand density threshold for 3D traction forces is related to the ability of cells to assemble adhesive complexes that engage the cytoskeleton. To test this explanation, we performed live cell imaging for cells expressing eGFP-vinculin [36] encapsulated in 4.5% PEG-4MAL hydrogels presenting either 0.5 mM or 2.0 mM RGD. Vinculin is an important cytoskeletal protein that links integrin-based adhesive complexes to the actin cytoskeleton to transfer force. For cells encapsulated in gels presenting 0.5 mM RGD, vinculin was mostly distributed diffusely throughout the cell (Fig. 4a). In contrast, cells in gels functionalized with 2.0 mM RGD exhibited distinct punctate vinculin complexes localized to the cell periphery and protrusions (Fig. 4b). These results indicate that a critical RGD density is required for vinculin localization to complexes at the cell periphery and protrusions, and this finding is consistent with the observed adhesive ligand density threshold for 3D traction forces.

3.4. Cells exert larger 3D forces with increasing matrix stiffness

We next examined how polymer density and matrix stiffness regulate cell morphology and mechanics within 3D matrices. It is well established that 2D cell spreading area and traction forces increase with elastic modulus on planar substrates, but it is not clear whether these relationships hold in 3D. Fibroblasts were cultured within PEG-4MAL hydrogels of 4.0%, 4.5%, 5.0%, and 6.0% polymer density at a constant 2.0 mM RGD density. The mean storage modulus for each formulation (Figs. 1d and 4.0%: 49 ± 8 Pa, 4.5%: 90 ± 20 Pa, 5.0%: 145 ± 32 Pa, 6.0%: 190 ± 50 Pa [mean ± SD]) spanned a range of moduli characteristic of biological matrices. After culturing cells in each gel formulation for 2 days (Fig. 5a–d), 3D TFM was performed on cells from each condition. Morphologically, cells were both larger and more polarized in stiffer gels (Fig. 5i and j). These results indicate a positive relationship between surrounding matrix stiffness and cell volume and polarity. Cells in the 6.0% gels demonstrated greater polarity compared to those in 4.0% and 5.0% gels. This result suggests that cells may spread more easily in stiffer 3D environments, as focal adhesions and stress fibers may develop more stably in stiffer conditions.

We next analyzed the deformation fields for each gel stiffness. As expected, cells in softer gels generated large matrix displacements and strain fields with relatively little stress, whereas those in stiffer gels required greater stress to generate smaller deformation fields (Fig. 5e–h). In 4.0% and 4.5% gels, displacement fields extend 40–50 μm along the principal axis of the cell, whereas those in 5.0% and 6.0% gels exhibit minimal displacements and strain. Conversely, large, centralized stress fields can be observed in both 5.0% and 6.0% gels, whereas little stress is observed in the 4.0% condition.

Consistent with these results, quantified matrix displacements and strains were inversely proportional to matrix stiffness. Mean and max displacements were significantly greater in 4% gels compared to those in 5.0% and 6.0% gels (Fig. 5k,l). A similar decreasing trend with increasing polymer density was seen for matrix strain (Fig. 5m,n). Notably, cells in 4.5% polymer density gels exhibited larger maximum strains than other groups, suggesting this intermediate stiffness value (~100 Pa) enables cells to deform the gel while generating larger total stress. This intermediate stiffness may provide an optimal mechanical environment for matrix modeling and migration.

Principal stress, traction stress, and strain energy were computed for each of the different stiffness conditions. In agreement with the polar contour plots, cell-generated stresses increased with matrix stiffness (Fig. 5o–q). In particular, cells in 5.0% gels produced larger mean and max stresses compared to those in 4.0% gels, while those in 6.0% gels were not different, but had smaller variance. This indicates a plateau in stress between 5.0% and 6.0% gels where cells are unable to produce higher stress. Interestingly, total principal stresses peaked at 4.5% gels without any differences in mean or max stress compared to all other groups (Fig. 5o–q), suggesting that cells are capable of generating the same magnitude of stress, but may require an intermediate stiffness to sustain such large stress throughout the cell. However, when comparing maximum tractions at the cell surface, there is a clear distinction between stresses generated at 4.0% polymer density and 5.0% (Fig. 5r–t). Strain energy and maximum strain energy density also show an increase between 4.0% and 4.5% polymer density, with cells in the 4.5% polymer density matrix displaying the highest maximum strain energy density with no differences in total strain energy between 4.5% compared to 5% and 6% PEG hydrogels (Fig. 5u–w). Taken together, these results demonstrate that cells apply 3D traction forces that increase with matrix stiffness, with corresponding decreases in matrix strain, until a plateau is reached, suggesting a stall in force generation.

3.5. Vinculin regulates 3D matrix deformation and force generation

After evaluating the effects of PEG-4MAL matrix properties (adhesive peptide density, matrix stiffness) on 3D force generation, we examined whether the mechanosensitive protein vinculin regulates 3D cellular force transmission. We used vinculin-null (NL) MEFs or vinculin-null cells stably expressing eGFP-vinculin (WT) [36]. As other groups have

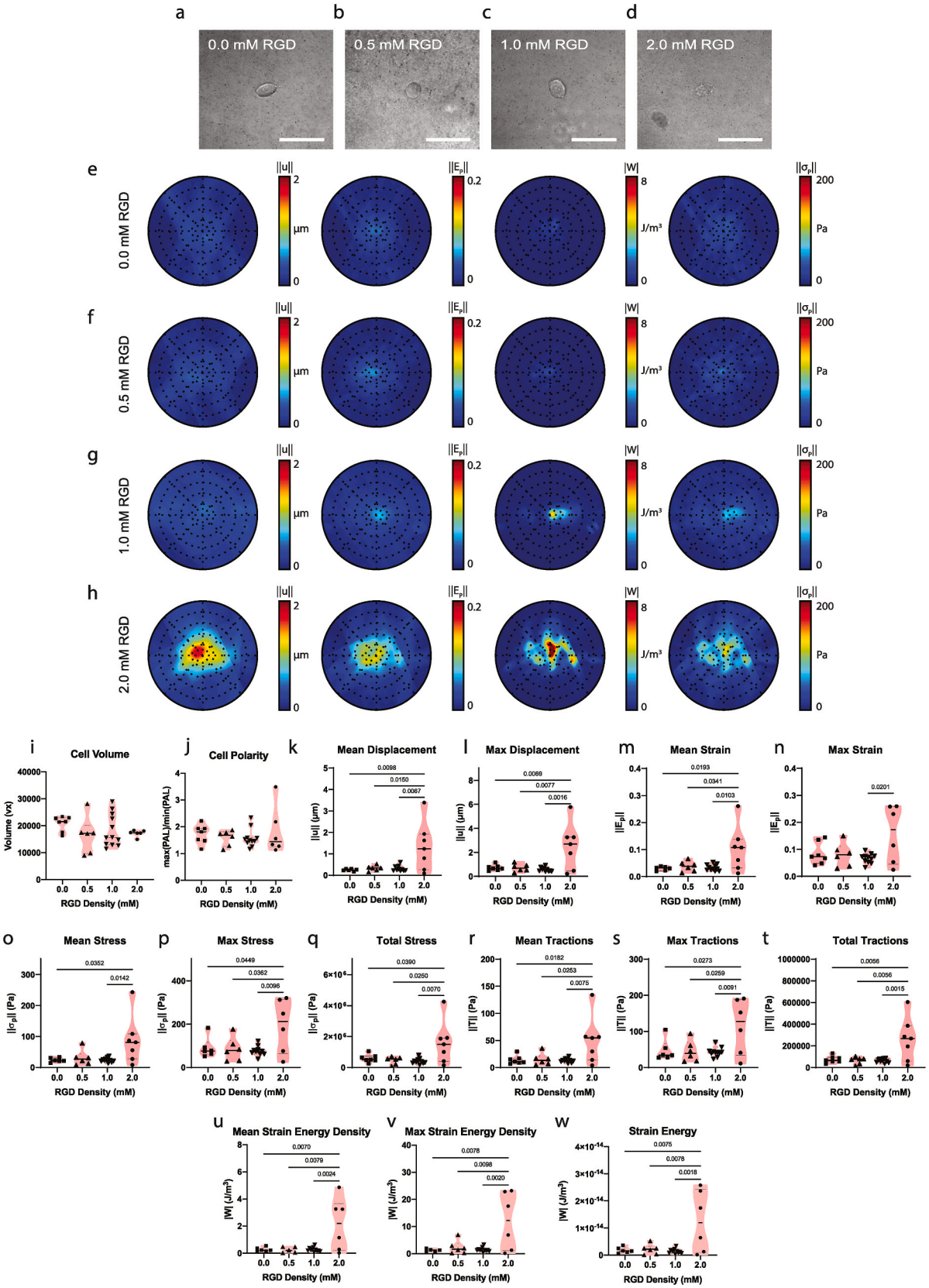

Fig. 3. Threshold adhesive ligand density is required for 3D forces. Images of cells encapsulated in 4.5% PEG-4MAL hydrogels containing (a) 0.0, (b) 0.5, (c) 1.0, and (d) 2.0 mM RGD, respectively. Scale bar 50 μm. (e–h) Polar contour plots displaying the average displacement, strain, stress, and strain energy density fields for cells in gels of varying ligand density. Graticules spaced at 10 μm apart. (i) Cell volume and (j) polarity for cells in PEG-4MAL gels presenting different RGD densities. (k) Mean and (l) maximum matrix displacements quantified within the cell volume. (m) Mean and (l) maximum matrix strain quantified within the cell volume. (o) Mean, (p) maximum, and (q) total matrix stresses quantified within the cell volume. (r) Mean, (s) maximum, and (t) total matrix tractions quantified at the cell surface. (u) Mean and (v) maximum strain energy density quantified within the cell volume. (w) Strain energy.

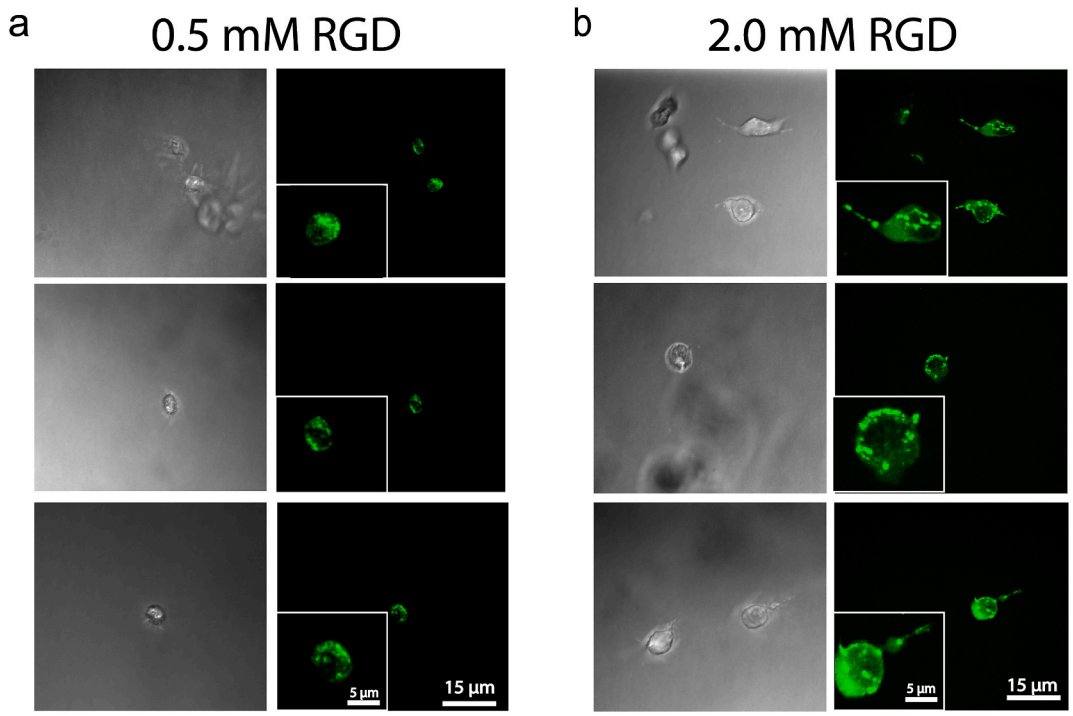

Fig. 4. Live cell imaging of eGFP-vinculin-expressing fibroblasts encapsulated in 4.5% PEG-4MAL hydrogels presenting either (a) 0.5 mM or (b) 2.0 mM RGD. For each cell, transmitted (left) and fluorescence (right) images are presented with a higher magnification image in the inset.

previously studied vinculin in 3D collagen gels [50,51], we first evaluated WT and NL cells within 1.5 mg/mL collagen gels (rat tail collagen). This collagen concentration was selected as it most closely matched the storage modulus of 4.0% PEG-4MAL hydrogels (Figure S6).

We first analyzed cells for their morphological differences (Fig. 6a and b). No differences in either cell volume or polarity were observed (Fig. 6c and d). This result was unexpected as previous studies reported that vinculin regulates both the size and shape of cells grown in similar microenvironmental conditions [50,51]. Differences in collagen formulation may account for these differences, as this prior work used a combination of rat and bovine collagen.

Despite the lack of morphological differences between WT and NL cells, qualitative differences are apparent in the polar contour plots (Fig. 6e and f). Small but distinct displacements and strains are present for WT cells, while no deformation fields are seen for NL cells. Stress fields were not computed for cells in collagen due to the complexity of the model that would be required to describe the mechanics at the cellular scale. Because collagen gels are comprised of a network of collagen fibers that are continually remodeled by fibroblasts, their mechanics are anisotropic, dynamic, and thus difficult to reliably describe [25,33].

Displacement and strains were quantified for WT and NL cells in collagen gels. As expected, WT cells generated significantly greater displacements and strains within 3D collagen gels (Fig. 6g–j). Maximum displacements and strains for WT cells were roughly twice as large as those produced in NL cells (Fig. 6h,j), indicating that vinculin is required for maximal force generation. These results demonstrate the importance of vinculin in 3D force generation in collagen gels.

We next examined whether vinculin is involved in force transmission within PEG-4MAL hydrogels. We used 4.0% PEG with 2.0 mM RGD to match the storage modulus of the collagen gels ($G'_{Collagen} = 44$ Pa, $G'_{PEG} = 49$ Pa [mean], Figure S6). Consistent with previous experiments, cells were cultured for 2 days prior to performing 3D TFM (Fig. 7a and b). Interestingly, there was a significant reduction in cell volume in NL cells compared to WT (Fig. 7e). This result likely reflects vinculin's role in recruiting and stabilizing actin stress fibers and reflecting a reduced ability of NL cells to spread in 3D, as observed in 2D for vinculin knockout or studies with blebbistatin [36]. On the other hand, WT and NL cells were similarly polarized (Fig. 7f).

Polar contour plots showed similarly shaped deformation fields for WT and NL cells, although the magnitude for NL cells was smaller (Fig. 7c and d). WT cells exhibited larger mean and maximum strains compared to NL cells (Fig. 7i and j), but no differences in matrix displacement were observed (Fig. 7g and h). Consistent with the role of vinculin in promoting higher traction forces in 2D [36], WT MEFs generated higher matrix mean/max/total stress values and total traction stresses compared to NL cells (Fig. 7k–p). WT cells also exhibited higher strain energy and strain energy density metrics (maximum and mean) than NL cells (Fig. 7q–s), reflecting an increased capacity to deform the matrix. These results demonstrate that vinculin regulates 3D matrix deformation and force generation in both synthetic and collagen gels.

4. Discussion

In this study, we established a platform integrating a well-defined synthetic hydrogel system with 3D TFM methodologies to evaluate deformation and force responses within synthetic microenvironments, providing insights that are not tractable using biological matrices because of the interdependence of biochemical and biophysical properties and complex architectures and mechanics. Although two groups have reported 3D TFM methodology applied to cells within PEG hydrogels [16,52], these studies did not evaluate the contributions of hydrogel properties to force generation. Our analysis included several metrics of 3D deformation and mechanics (displacement, strain, stress, traction, and strain energy) for a more robust assessment of the biological responses. Although it may be expected that deformation/strain and traction/stress metrics should exhibit consistent trends as they are related by simple continuum mechanics, we note significant technical challenges associated with performing these analyses in live single cells and at high 3D spatial resolution, which may result in high experimental variance which limits direct correspondence between deformation/-strain and traction/stress metrics. Therefore, our conclusions are based

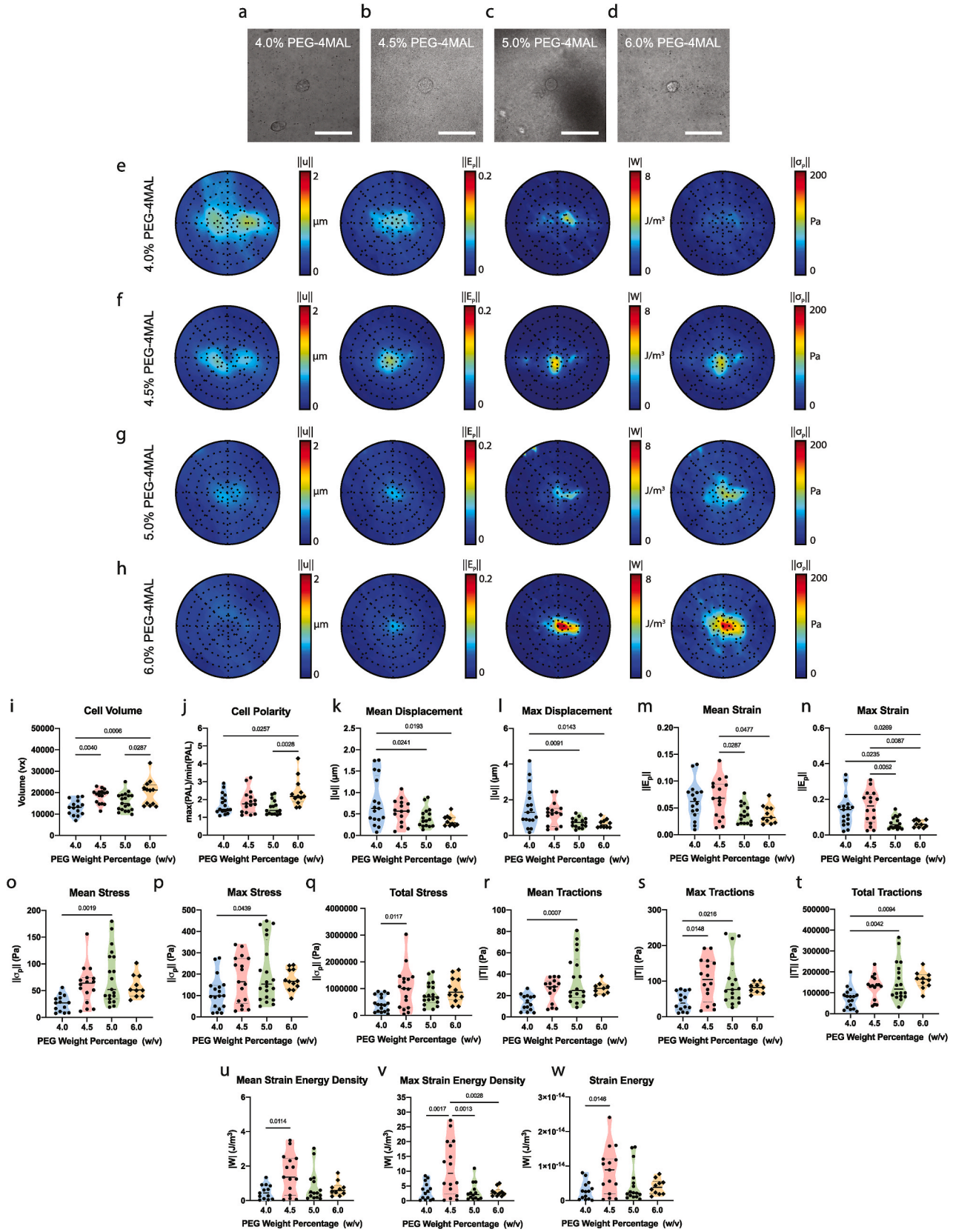

Fig. 5. Fibroblasts exert larger 3D forces with increasing matrix stiffness. Images of cells MEFs encapsulated in (a) 4.0%, (b) 4.5%, (c) 5.0%, and (d) 6.0% PEG-4MAL hydrogels containing 2.0 mM RGD, respectively. Scale bar = 50 μm. (e–h) Polar contour plots displaying the average displacement, strain, stress, and strain energy density fields for cells in gels of varying polymer density. Graticules spaced at 10 μm apart. (i) Cell volume and (j) polarity within gels of varying polymer density. (k) Mean and (l) maximum matrix displacements quantified within the cell volume. (m) Mean and (n) maximum matrix strain quantified within the cell volume. (o) Mean, (p) maximum, and (q) total matrix stresses quantified within the cell volume. (r) Mean, (s) maximum, and (t) total matrix tractions quantified at the cell surface. (u) Mean and (v) maximum strain energy density quantified within the cell volume. (w) Strain energy.

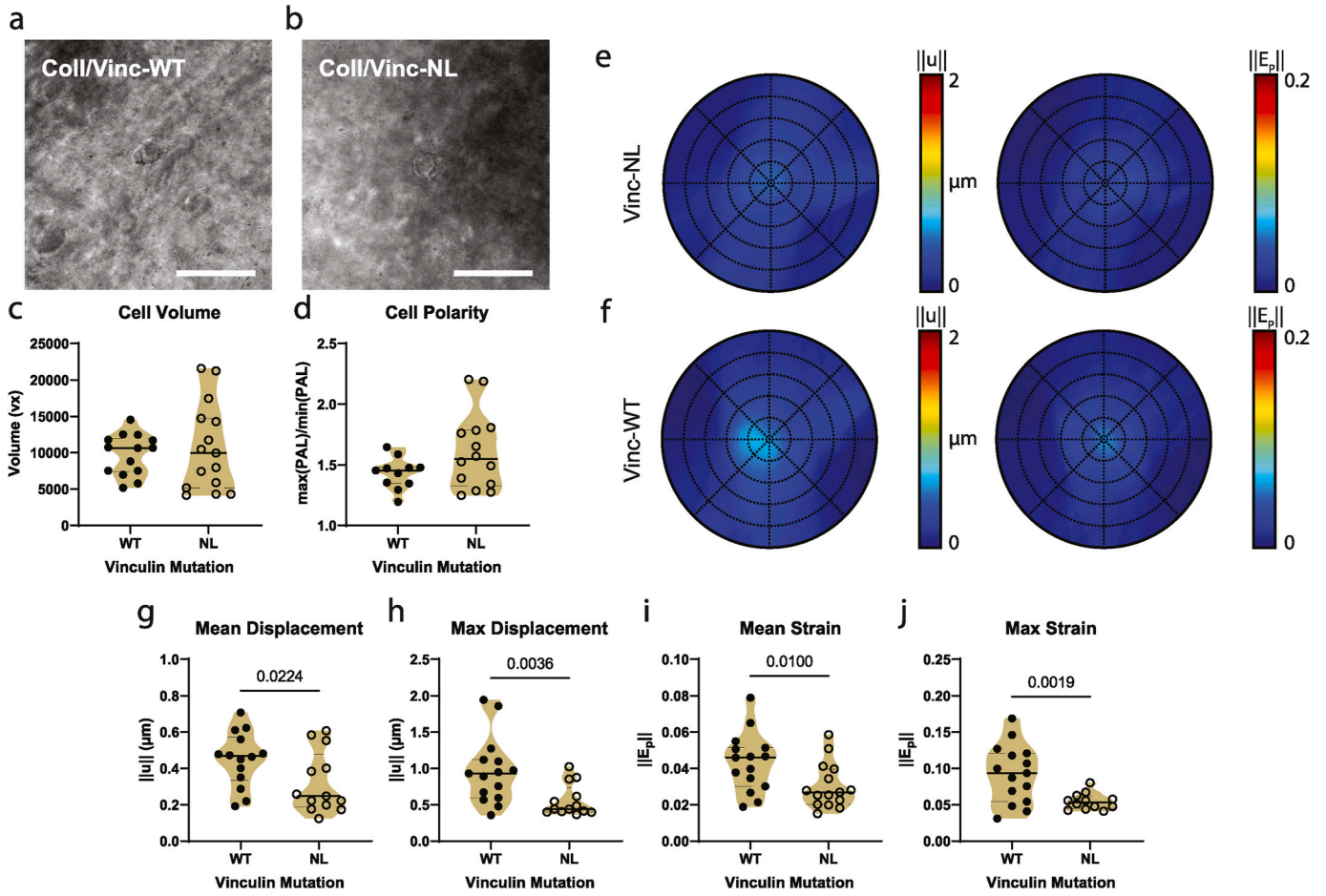

Fig. 6. Vinculin is required for generation of matrix displacements and strain 3D collagen gels. Images of (a) vinculin-null fibroblasts re-expressing vinculin (WT) and (b) vinculin-null fibroblasts encapsulated in 1.5 mg/mL collagen gels. Scale bar = 50 μm. (c) Cell volume and (d) polarity of WT and NL cells. (e,f) Polar contour plots displaying the average displacement and strain fields for WT and NL cells. Graticules spaced at 10 μm apart. (g) Mean and (h) maximum matrix displacements quantified within the cell volume. (i) Mean and (j) maximum matrix strain quantified within the cell volume.

on interpretation of the aggregate of the various metrics observed to provide a more robust assessment of the biological responses. In the present work, we dissected the contributions of mechanical (stiffness) and biochemical (adhesive peptide density) properties of the extracellular microenvironment to 3D force generation and showed that both hydrogel properties modulate the cell's ability to generate 3D traction forces and deform its surrounding matrix. To validate our 3D TFM methodology, we assessed RDG non-adhesive peptide controls to determine the effects of cell secreted proteins (proteases and ECM) and collagen hydrogels to show alignment with previous 3D TFM work and draw comparisons between synthetic and biological matrices. We demonstrated that Rho kinase-regulated actomyosin contractility and vinculin expression are necessary for the generation of 3D traction forces in synthetic hydrogels, consistent with observations in biological matrices [23,53]. This research establishes a tunable platform for the study of mechanobiology and provides new insights into how cells sense and transmit forces in 3D. However, technical limitations of the 3D TFM platform include the 3D optical resolution of the equipment used and the biological variance of 3D deformations at the single cell resolution. Additionally, cells must be seeded at a sufficiently low density to minimize confounding cell-cell interaction which may alter the cell morphology and behavior. Although cell density is limited by the 3D TFM methodology, this value was held constant across all experimental groups including both collagen and PEG-4MAL hydrogels and should not be a confounding factor in the comparison and analysis of the data. The PEG-4MAL hydrogel is also modeled as a neo-Hookean material due to the non-linear, isotropic, and homogenous characteristics of the material but different material assumptions could motivate the use of other models including a Hookean or Kelvin-Voigt model. Additionally, bulk rheology measurements of G′ and G″ was used to characterize all of our PEG-4MAL and collagen hydrogels but may not accurately determine the local properties perceived by the cells, which is a general limitation across most TFM studies and remains an active area of research beyond the scope of the data presented.

We found that adhesive peptide density plays a critical role in cellular force production and matrix deformation. Remarkably, 3D traction forces did not increase monotonically with adhesive peptide density, but instead exhibited a critical threshold of adhesive peptide density between 1.0 and 2.0 mM RGD for step-like increases in 3D force. This result indicates that a critical density of adhesive peptide is required for sufficient integrin clusters to form and the cellular contractile machinery to engage with the matrix ligand and generate force. Indeed, prior studies with nanopatterned RGD peptides on planar supports revealed a minimum spacing of adhesive ligand required for focal adhesion assembly and actin stress fiber formation [54–56]. For example, Spatz and colleagues reported the minimum RGD spacing necessary for integrin activation to lie between 58 and 73 nm [55]. Based on rubber elasticity theory and rheology [32], we estimate the mesh size for a 4.5% PEG-4MAL hydrogel to be ~40 nm. For a 4.5% PEG-4MAL hydrogel presenting 2.0 mM RGD, there is a 1 RGD:1.125 PEG-4MAL macromer ratio, yielding an RGD spacing of ~45 nm. Because this spacing is below the critical spacing reported by Spatz et al. we predict sufficient integrin clustering and cytoskeleton engagement, which is consistent with the experimental results of high 3D traction

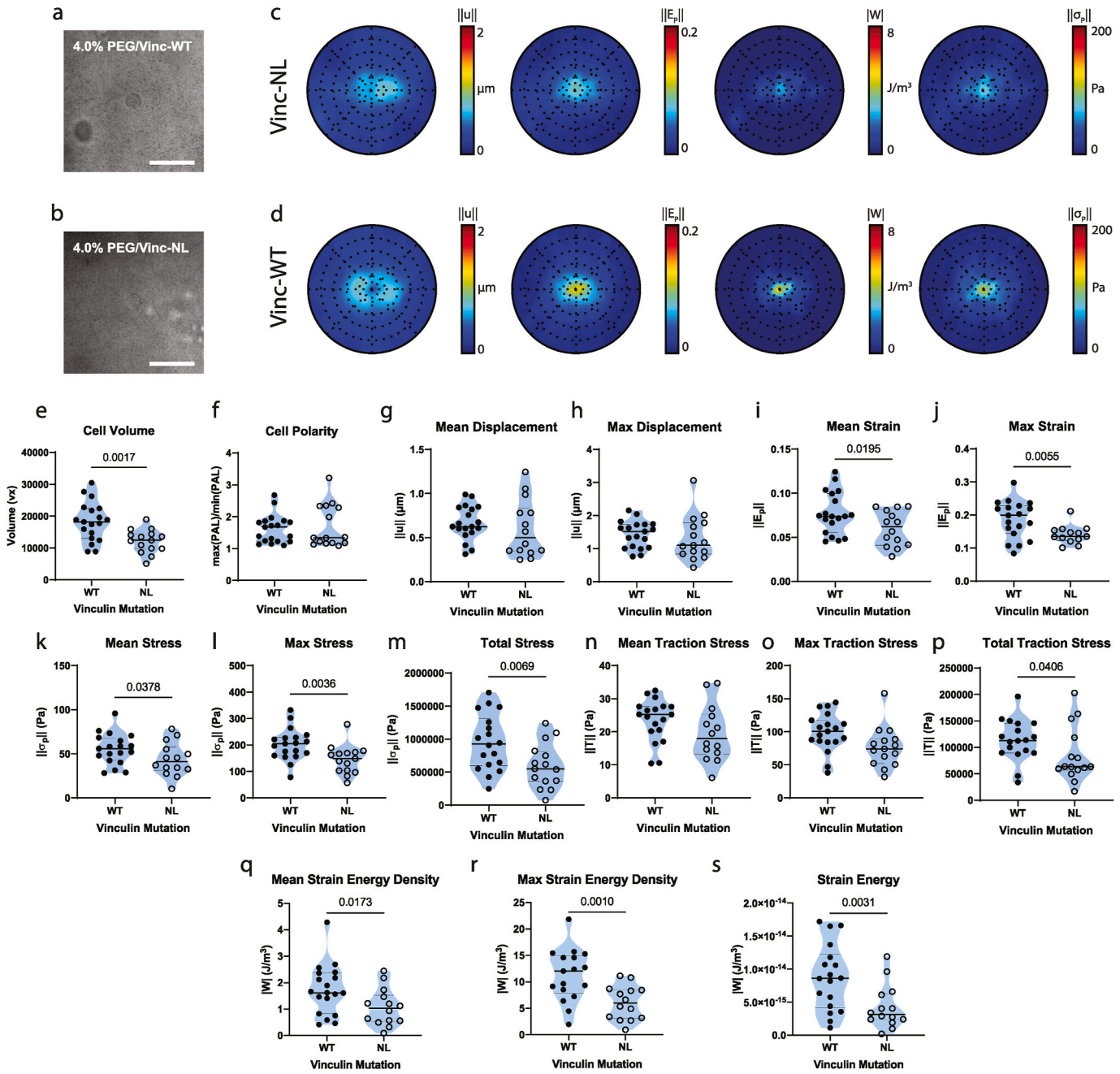

Fig. 7. Vinculin regulates 3D matrix deformation and force generation in synthetic hydrogels. Images of (a) vinculin-null fibroblasts re-expressing vinculin (WT) and (b) vinculin-null fibroblasts encapsulated in 4.0% PEG-4MAL hydrogels presenting 2.0 mM RGD. Scale bar = 50 μm. (c,d) Polar contour plots displaying the average displacement and strain fields for NL and WT cells. Graticules spaced at 10 μm apart. (e) Cell volume and (f) polarity for WT and NL cells within PEG-4MAL gels. (g) Mean and (h) maximum matrix displacements quantified within the cell volume. (i) Mean and (j) maximum matrix strain quantified within the cell volume. (k) Mean, (l) maximum, and (m) total matrix stresses quantified within the cell volume. (n) Mean, (o) maximum, and (p) total matrix tractions quantified at the cell surface. (q) Mean and (r) maximum strain energy density quantified within the cell volume. (s) Strain energy.

forces. For a 4.5% PEG-4MAL hydrogel presenting 1.0 mM RGD, the RGD spacing becomes ~90 nm. Because this spacing is above the critical spacing, we expect inefficient integrin clustering and cytoskeleton engagement, which is also consistent with the observed low 3D traction forces for this gel formulation. In support of this model, we observed that a critical RGD density is required for vinculin localization to complexes at the cell periphery and protrusions. This finding provides insights on important biochemical design criteria for the engineering of synthetic cell microenvironments.

We also found that polymer density, and therefore matrix stiffness in the range of 40–200 Pa, independent of adhesion ligand density regulates cellular morphology and 3D traction forces and matrix deformation. Cell volume and polarity increased with PEG hydrogel stiffness. We attribute this relationship to the ability of the cell to generate larger forces and extend processes in the stiffer matrices. This finding is consistent with observations on planar supports that cell size and polarity increase with substrate stiffness [57,58]. However, in other 3D contexts, particularly in fibrous materials like collagen gels and electrospun nanofibers, the opposite trends were reported [12,25]. The disparity in trends between the mesh-based PEG hydrogel system and the fibrous matrices likely reflects differences in ECM architecture, local ligand density, and physical cell confinement. Matrix displacements and

strains decreased with matrix stiffness whereas stresses and tractions increased with matrix stiffness until reaching constant values at higher stiffness values. Strain energy peaked at an intermediate stiffness of ~100 Pa (4.5% PEG-4MAL). The inverse trends between matrix displacement/strains vs. stress/tractions is expected as matrix deformation and force are coupled by the matrix mechanical properties (e.g., stiffness). Steinwachs et al. reported decreasing matrix displacements but no changes in total force with increasing collagen concentration for cells in collagen gels [25]. However, when comparing cells with a similar aspect ratio Steinwachs et al. observed an increase in contractility in 1.2 mg/mL collagen gels compared to 0.6 mg/mL collagen gels. The interpretation of this result is limited by concentration-dependent changes in adhesive ligand density and collagen fiber/gel structure. Notably, we observed the highest levels of stress/tractions/strain energy density for the 4.5–5% PEG-4MAL formulations. These results indicate an intermediate stiffness range (~80–150 Pa) that supports the generation of maximal 3D forces. We attribute the lack of further increases in force with increasing matrix stiffness beyond this optimal value to an inability of the cell to generate further levels of force (i.e., a stall in force generation). However, we cannot rule out that higher 3D forces could be developed in matrices with higher adhesive peptide density or different adhesive peptides. Furthermore, it is possible that cell confinement in the 6% PEG-4MAL gels contributes to the observed plateau in 3D force generation. Burdick and colleagues demonstrated that covalently-crosslinked hyaluronic acid hydrogels that permit (restrict) cell-mediated degradation supported high (low) degrees of cell spreading and high (low) tractions independently of matrix stiffness [42]. However, we observed increased cell volume and polarity in the 6% PEG-4MAL gels, suggesting that the plateau in 3D forces is not primarily due to limited cell confinement. Further studies are necessary to establish the mechanisms for the force stalling response at high matrix stiffness values and to understand the intracellular molecular mechanisms for 3D force generation within these synthetic microenvironments.

5. Conclusion

In this study, we established a platform integrating a well-defined synthetic hydrogel system with 3D TFM methodologies to evaluate cellular forces within synthetic microenvironments, providing insights that are not tractable using biological matrices. We showed that both hydrogel mechanical properties and adhesive peptide density modulate the cell's ability to generate 3D traction forces and deform its surrounding matrix. We also demonstrated that Rho kinase-regulated actomyosin contractility and vinculin expression are necessary for the generation of 3D traction forces in this synthetic microenvironment, consistent with observations in biological matrices. This research establishes a tunable platform for the study of mechanobiology and provides new insights into how cells sense and transmit forces in 3D.

Credit author statement

Mark Colasurdo: Conceptualization, Methodology, Software, Formal analysis, Investigation, Data curation, Writing-Original **Elisa Nieves**: Investigation, Formal analysis, Writing – review & editing **Marc Fernández-Yagüe**: Investigation **Christian Franck**: Conceptualization, Methodology, Software, Resources **Andrés García**: Conceptualization, Methodology, Formal analysis, Writing – review & editing, Supervision, Project administration, Funding acquisition.

Declaration of competing interest

The authors declare that they have no known competing financial interests or personal relationships that could have appeared to influence the work reported in this paper.

Data availability

Data will be made available on request.

Acknowledgements

The authors acknowledge helpful discussions and recommendations from Elijah N. Holland (GT), Cheng Zhu (GT), Jennifer E. Curtis (GT), Dennis Zhou (GT), and Khalid Salaita (Emory Univ). This work was funded by the National Institutes of Health (R01 EB024322 [A.J.G.], T32 GM008433 [M.C.]), National Science Foundation Graduate Fellowships (DGE-1650044 [M.C], DGE- 2039655 [E.B.N.]), and Marie Skłodowska-Curie Postdoctoral Fellowship (M.A.F.-Y.).

Appendix A. Supplementary data

Supplementary data to this article can be found online at https://doi.org/10.1016/j.biomaterials.2022.121710.

References

[1] D.E. Discher, L. Smith, S. Cho, M. Colasurdo, A.J. Garcia, S. Safran, Matrix mechanosensing: from scaling concepts in 'omics data to mechanisms in the nucleus, regeneration, and cancer, Annu. Rev. Biophys. 46 (2017) 295–315.
[2] K.A. Jansen, P. Atherton, C. Ballestrem, Mechanotransduction at the cell-matrix interface, Semin. Cell Dev. Biol. 71 (2017) 75–83.
[3] Y. Chen, L. Ju, M. Rushdi, C. Ge, C. Zhu, Receptor-mediated cell mechanosensing, Mol. Biol. Cell 28 (23) (2017) 3134–3155.
[4] M.A. Wozniak, C.S. Chen, Mechanotransduction in development: a growing role for contractility, Nat. Rev. Mol. Cell Biol. 10 (1) (2009) 34–43.
[5] S. Kumar, V.M. Weaver, Mechanics, malignancy, and metastasis: the force journey of a tumor cell, Cancer Metastasis Rev. 28 (1–2) (2009) 113–127.
[6] F. Broders-Bondon, T.H. Nguyen Ho-Bouldoires, M.E. Fernandez-Sanchez, E. Farge, Mechanotransduction in tumor progression: the dark side of the force, J. Cell Biol. 217 (5) (2018) 1571–1587.
[7] K.H. Vining, D.J. Mooney, Mechanical forces direct stem cell behaviour in development and regeneration, Nat. Rev. Mol. Cell Biol. 18 (12) (2017) 728–742.
[8] N. Huebsch, P.R. Arany, A.S. Mao, D. Shvartsman, O.A. Ali, S.A. Bencherif, J. Rivera-Feliciano, D.J. Mooney, Harnessing traction-mediated manipulation of the cell/matrix interface to control stem-cell fate, Nat. Mater. 9 (6) (2010) 518–526.
[9] C. Yang, M.W. Tibbitt, L. Basta, K.S. Anseth, Mechanical memory and dosing influence stem cell fate, Nat. Mater. 13 (6) (2014) 645–652.
[10] C.M. Madl, S.C. Heilshorn, H.M. Blau, Bioengineering strategies to accelerate stem cell therapeutics, Nature 557 (7705) (2018) 335–342.
[11] A.D. Doyle, F.W. Wang, K. Matsumoto, K.M. Yamada, One-dimensional topography underlies three-dimensional fibrillar cell migration, J. Cell Biol. 184 (4) (2009) 481–490.
[12] B.M. Baker, C.S. Chen, Deconstructing the third dimension: how 3D culture microenvironments alter cellular cues, J. Cell Sci. 125 (Pt 13) (2012) 3015–3024.
[13] S.I. Fraley, Y. Feng, R. Krishnamurthy, D.H. Kim, A. Celedon, G.D. Longmore, D. Wirtz, A distinctive role for focal adhesion proteins in three-dimensional cell motility, Nat. Cell Biol. 12 (6) (2010) 598–604.
[14] M.J. Siedlik, V.D. Varner, C.M. Nelson, Pushing, pulling, and squeezing our way to understanding mechanotransduction, Methods 94 (2016) 4–12.
[15] C. Franck, S.A. Maskarinec, D.A. Tirrell, G. Ravichandran, Three-dimensional traction force microscopy: a new tool for quantifying cell-matrix interactions, PLoS One 6 (3) (2011), e17833.
[16] W.R. Legant, J.S. Miller, B.L. Blakely, D.M. Cohen, G.M. Genin, C.S. Chen, Measurement of mechanical tractions exerted by cells in three-dimensional matrices, Nat. Methods 7 (12) (2010) 969–971.
[17] M. Condor, J. Steinwachs, C. Mark, J.M. Garcia-Aznar, B. Fabry, Traction force microscopy in 3-dimensional extracellular matrix networks, Curr. Protoc. Cell Biol. 75 (2017) 10 22 1–10 22 20.
[18] J. Barrasa-Fano, A. Shapeti, J. de Jong, A. Ranga, J.A. Sanz-Herrera, H. Van Oosterwyck, Advanced in silico validation framework for three-dimensional traction force microscopy and application to an in vitro model of sprouting angiogenesis, Acta Biomater. 126 (2021) 326–338.
[19] A. Izquierdo-Alvarez, D.A. Vargas, A. Jorge-Penas, R. Subramani, M.M. Vaeyens, H. Van Oosterwyck, Spatiotemporal analyses of cellular tractions describe subcellular effect of substrate stiffness and coating, Ann. Biomed. Eng. 47 (2) (2019) 624–637.
[20] J.A. Sanz-Herrera, J. Barrasa-Fano, M. Condor, H. Van Oosterwyck, Inverse method based on 3D nonlinear physically constrained minimisation in the framework of traction force microscopy, Soft Matter 17 (45) (2021) 10210–10222.
[21] L. Hazlett, A.K. Landauer, M. Patel, H.A. Witt, J. Yang, J.S. Reichner, C. Franck, Epifluorescence-based three-dimensional traction force microscopy, Sci. Rep. 10 (1) (2020), 16599.

[22] S. Hervas-Raluy, M.J. Gomez-Benito, C. Borau-Zamora, M. Condor, J.M. Garcia-Aznar, A new 3D finite element-based approach for computing cell surface tractions assuming nonlinear conditions, PLoS One 16 (4) (2021), e0249018.
[23] L.M. Owen, A.S. Adhikari, M. Patel, P. Grimmer, N. Leijnse, M.C. Kim, J. Notbohm, C. Franck, A.R. Dunn, A cytoskeletal clutch mediates cellular force transmission in a soft, three-dimensional extracellular matrix, Mol. Biol. Cell 28 (14) (2017) 1959–1974.
[24] S.E. Leggett, M. Patel, T.M. Valentin, L. Gamboa, A.S. Khoo, E.K. Williams, C. Franck, I.Y. Wong, Mechanophenotyping of 3D multicellular clusters using displacement arrays of rendered tractions, Proc. Natl. Acad. Sci. U. S. A. 117 (11) (2020) 5655–5663.
[25] J. Steinwachs, C. Metzner, K. Skodzek, N. Lang, I. Thievessen, C. Mark, S. Munster, K.E. Aifantis, B. Fabry, Three-dimensional force microscopy of cells in biopolymer networks, Nat. Methods 13 (2) (2016) 171–176.
[26] T.M. Koch, S. Munster, N. Bonakdar, J.P. Butler, B. Fabry, 3D Traction forces in cancer cell invasion, PLoS One 7 (3) (2012), e33476.
[27] S.R. Caliari, J.A. Burdick, A practical guide to hydrogels for cell culture, Nat. Methods 13 (5) (2016) 405–414.
[28] E.A. Phelps, N.O. Enemchukwu, V.F. Fiore, J.C. Sy, N. Murthy, T.A. Sulchek, T. H. Barker, A.J. Garcia, Maleimide cross-linked bioactive PEG hydrogel exhibits improved reaction kinetics and cross-linking for cell encapsulation and in situ delivery, Adv. Mater. 24 (1) (2012) 64–70, 2.
[29] K.S. Anseth, H.A. Klok, Click chemistry in biomaterials, Nanomed. Drug Deliv. Biomacromolecules 17 (1) (2016) 1–3.
[30] M.P. Lutolf, H.M. Blau, Artificial stem cell niches, Adv. Mater. 21 (32–33) (2009) 3255–3268.
[31] M. Lutolf, J. Hubbell, Synthetic biomaterials as instructive extracellular microenvironments for morphogenesis in tissue engineering, Nat. Biotechnol. 23 (1) (2005) 47–55.
[32] A.Y. Clark, K.E. Martin, J.R. Garcia, C.T. Johnson, H.S. Theriault, W.M. Han, D. W. Zhou, E.A. Botchwey, A.J. Garcia, Integrin-specific hydrogels modulate transplanted human bone marrow-derived mesenchymal stem cell survival, engraftment, and reparative activities, Nat. Commun. 11 (1) (2020) 114.
[33] J. Toyjanova, E. Bar-Kochba, C. López-Fagundo, J. Reichner, D. Hoffman-Kim, C. Franck, High resolution, large deformation 3D traction force microscopy, PLoS One 9 (4) (2014), e90976.
[34] S.A. Maskarinec, C. Franck, D.A. Tirrell, G. Ravichandran, Quantifying cellular traction forces in three dimensions, Proc. Natl. Acad. Sci. U. S. A. 106 (52) (2009) 22108–22113.
[35] J. Toyjanova, E. Hannen, E. Bar-Kochba, E.M. Darling, D.L. Henann, C. Franck, 3D Viscoelastic traction force microscopy, Soft Matter 10 (40) (2014) 8095–8106.
[36] D.W. Dumbauld, T.T. Lee, A. Singh, J. Scrimgeour, C.A. Gersbach, E.A. Zamir, J. Fu, C.S. Chen, J.E. Curtis, S.W. Craig, A.J. Garcia, How vinculin regulates force transmission, Proc. Natl. Acad. Sci. U. S. A. 110 (24) (2013) 9788–9793.
[37] D. Zhou, A.J. Garcia, Measurement systems for cell adhesive forces, J. Biomech. Eng. 137 (2014) 020908, https://doi.org/10.1115/1.4029210.
[38] W.J. Polacheck, C.S. Chen, Measuring cell-generated forces: a guide to the available tools, Nat. Methods 13 (5) (2016) 415–423.
[39] E.A. Phelps, D.M. Headen, W.R. Taylor, P.M. Thule, A.J. García, Vasculogenic bio-synthetic hydrogel for enhancement of pancreatic islet engraftment and function in type 1 diabetes, Biomaterials 34 (19) (2013) 4602–4611.
[40] K. Bott, Z. Upton, K. Schrobback, M. Ehrbar, J.A. Hubbell, M.P. Lutolf, S.C. Rizzi, The effect of matrix characteristics on fibroblast proliferation in 3D gels, Biomaterials 31 (32) (2010) 8454–8464.
[41] M. Caiazzo, Y. Okawa, A. Ranga, A. Piersigilli, Y. Tabata, M.P. Lutolf, Defined three-dimensional microenvironments boost induction of pluripotency, Nat. Mater. 15 (3) (2016) 344–352.
[42] S. Khetan, M. Guvendiren, W.R. Legant, D.M. Cohen, C.S. Chen, J.A. Burdick, Degradation-mediated cellular traction directs stem cell fate in covalently crosslinked three-dimensional hydrogels, Nat. Mater. 12 (5) (2013) 458–465.
[43] M. Morsch, R.A. Radford, E.K. Don, A. Lee, E. Hortle, N.J. Cole, R.S. Chung, Triggering cell stress and death using conventional UV laser confocal microscopy, JoVE : JoVE 120 (2017).
[44] L. Soustelle, B. Aigouy, M.L. Asensio, A. Giangrande, UV laser mediated cell selective destruction by confocal microscopy, Neural Dev. 3 (2008) 11.
[45] M.C. Kim, C. Kim, L. Wood, D. Neal, R.D. Kamm, H.H. Asada, Integrating focal adhesion dynamics, cytoskeleton remodeling, and actin motor activity for predicting cell migration on 3D curved surfaces of the extracellular matrix, Integr. Biol. (Camb) 4 (11) (2012) 1386–1397.
[46] T. Kim, W. Hwang, R.D. Kamm, Dynamic role of cross-linking proteins in actin rheology, Biophys. J. 101 (7) (2011) 1597–1603.
[47] J. Kolega, Phototoxicity and photoinactivation of blebbistatin in UV and visible light, Biochem. Biophys. Res. Commun. 320 (3) (2004) 1020–1025.
[48] A. Engler, L. Bacakova, C. Newman, A. Hategan, M. Griffin, D. Discher, Substrate compliance versus ligand density in cell on gel responses, Biophys. J. 86 (1 Pt 1) (2004) 617–628.
[49] E.A. Cavalcanti-Adam, T. Volberg, A. Micoulet, H. Kessler, B. Geiger, J.P. Spatz, Cell spreading and focal adhesion dynamics are regulated by spacing of integrin ligands, Biophys. J. 92 (8) (2007) 2964–2974.
[50] I. Thievessen, N. Fakhri, J. Steinwachs, V. Kraus, R.S. McIsaac, L. Gao, B.C. Chen, M.A. Baird, M.W. Davidson, E. Betzig, R. Oldenbourg, C.M. Waterman, B. Fabry, Vinculin is required for cell polarization, migration, and extracellular matrix remodeling in 3D collagen, Faseb. J. 29 (11) (2015) 4555–4567.
[51] A. Rahman, S.P. Carey, C.M. Kraning-Rush, Z.E. Goldblatt, F. Bordeleau, M. C. Lampi, D.Y. Lin, A.J. Garcia, C.A. Reinhart-King, Vinculin regulates directionality and cell polarity in 2D, 3D matrix and 3D microtrack migration, Mol. Biol. Cell 27 (2016), 1431-1411.
[52] O.A. Banda, C.R. Sabanayagam, J.H. Slater, Reference-free traction force microscopy platform fabricated via two-photon laser scanning lithography enables facile measurement of cell-generated forces, ACS Appl. Mater. Interfaces 11 (20) (2019) 18233–18241.
[53] C.T. Mierke, P. Kollmannsberger, D.P. Zitterbart, G. Diez, T.M. Koch, S. Marg, W. H. Ziegler, W.H. Goldmann, B. Fabry, Vinculin facilitates cell invasion into three-dimensional collagen matrices, J. Biol. Chem. 285 (17) (2010) 13121–13130.
[54] S.P. Massia, J.A. Hubbell, An RGD spacing of 440 nm is sufficient for integrin alpha v beta 3-mediated fibroblast spreading and 140 nm for focal contact and stress fiber formation, JCB (J. Cell Biol.) 114 (1991) 1089–1100.
[55] M. Arnold, E.A. Cavalcanti-Adam, R. Glass, J. Blummel, W. Eck, M. Kantlehner, H. Kessler, J.P. Spatz, Activation of integrin function by nanopatterned adhesive interfaces, ChemPhysChem 5 (3) (2004) 383–388.
[56] G. Maheshwari, G. Brown, D.A. Lauffenburger, A. Wells, L.G. Griffith, Cell adhesion and motility depend on nanoscale RGD clustering, J. Cell Sci. 113 (2000) 1677–1686.
[57] T. Yeung, P.C. Georges, L.A. Flanagan, B. Marg, M. Ortiz, M. Funaki, N. Zahir, W. Ming, V. Weaver, P.A. Janmey, Effects of substrate stiffness on cell morphology, cytoskeletal structure, and adhesion, Cell Motil Cytoskeleton 60 (1) (2005) 24–34.
[58] J.P. Califano, C.A. Reinhart-King, Substrate stiffness and cell area predict cellular traction stresses in single cells and cells in contact, Cell. Mol. Bioeng. 3 (1) (2010) 68–75.